Thermal photon emission from quark-gluon plasma: 1+1D magnetohydrodynamics results*

Jie Xiong (熊杰)[1] Xiang Fan (樊翔)[2] Jing Jing (靖晶)[1] Weishan Yang (杨维山)[1]
Duan She (佘端)[3] Ze-Fang Jiang (江泽方)[1,2†]

[1]Department of Physics and Electronic-Information Engineering, Hubei Engineering University, Xiaogan 432000, China
[2]Institute of Particle Physics and Key Laboratory of Quark and Lepton Physics (MOE), Central China Normal University, Wuhan 430079, China
[3]Institute of Physics, Henan Academy of Sciences, Zhengzhou 450046, China

Abstract: We investigate thermal photon production in the quark-gluon plasma (QGP) under strong magnetic fields using a magnetohydrodynamic (MHD) framework. We employ relativistic ideal fluid dynamics under the non-resistive approximation by adopting the Bjorken flow model with power-law decaying magnetic fields $\mathbf{B}(\tau)=\mathbf{B}_0(\tau_0/\tau)^a$, span> a controls the decay rate, $B_0=\sqrt{\sigma}T_0^2$, and σ characterizes the initial field strength. The resulting QGP temperature evolution exhibits distinct a- and σ-dependent behaviors. Thermal photon production rates are calculated for three dominant processes: Compton scattering with $q\bar{q}$ annihilation (C+A), bremsstrahlung (Brems), and $q\bar{q}$ annihilation with additional scattering (A+S). These rates are integrated over the space-time volume to obtain the photon transverse momentum (p_T) spectrum. Our results demonstrate that increasing a enhances photon yields across all p_T, with $a\to\infty$ (super-fast decay) providing an upper bound. For $a=2/3$, a larger σ suppresses yields through accelerated cooling, whereas for $a\to\infty$, a larger σ enhances yields via prolonged thermal emission. Low-p_T photons receive significant contributions from all QGP evolution stages, while high-p_T photons originate predominantly from early times. The central rapidity region ($y=0$) dominates the total yield. This work extends the photon yield studies to the MHD regime under strong magnetic fields, clarifying the magnetic field effects on QGP electromagnetic signatures and establishing foundations for future investigations of magnetization and dissipative phenomena.

Keywords: quark-gluon plasma, relativistic heavy ion collisions, magnetohydrodynamics, thermal photon

DOI: 10.1088/1674-1137/ae3313 **CSTR:** 32044.14.ChinesePhysicsC.50044105

I. INTRODUCTION

Heavy-ion collisions at the relativistic heavy ion collider (RHIC) and large hadron collider (LHC) provide a unique platform to study quark-gluon plasma (QGP), which is a deconfined state of nuclear matter created under extreme temperature and pressure conditions [1, 2]. A striking feature of these collisions is the generation of extremely strong magnetic fields, with magnitudes ranging from 10^{18} to 10^{20} Gauss, induced by the rapid motion of charged spectator nucleons [3−5]. These strong magnetic fields are expected to modulate QGP dynamics through various mechanisms [6−12], including quantum anomaly-induced phenomena such as the chiral magnetic effect, chiral separation effect, and chiral magnetic wave [13−25]. Despite significant experimental efforts to detect these effects at RHIC and LHC [26−32], extracting their signatures from collective flow backgrounds remains a critical challenge.

Relativistic hydrodynamics has emerged as a powerful tool to describe QGP evolution, successfully interpreting experimental observables such as harmonic flows and global polarization in non-central collisions [33−44]. The dynamic interplay between electromagnetic fields and QGP requires solving full (3+1)-dimensional relativistic magnetohydrodynamic (MHD) equations [45−47]. Lattice quantum chronodynamics (QCD) calculations confirm that the QGP exhibits a temperature-dependent electrical conductivity σ_{el} [48, 49]. However, the interaction

Received 20 October 2025; Accepted 5 January 2026; Accepted manuscript online 6 January 2026

* Supported by the National Natural Science Foundation of China (NSFC) (12305138). Duan She's research is funded by the Startup Research Fund of Henan Academy of Sciences (231820058) and the 2024 Henan Province International Science and Technology Cooperation Projects (242102521068)

† E-mail: jiangzf@mails.ccnu.edu.cn

Content from this work may be used under the terms of the Creative Commons Attribution 3.0 licence. Any further distribution of this work must maintain attribution to the author(s) and the title of the work, journal citation and DOI. Article funded by SCOAP[3] and published under licence by Chinese Physical Society and the Institute of High Energy Physics of the Chinese Academy of Sciences and the Institute of Modern Physics of the Chinese Academy of Sciences and IOP Publishing Ltd

between initial magnetic fields and the QGP medium [50−53], along with the subsequent evolution of the field, remains incompletely understood. Recent advances have explored electromagnetic effects within hydrodynamic frameworks [54], including 1+1 dimensional Bjorken flow in ideal MHD, where energy density evolves via the "frozen-flux theorem" [55−58], and extensions incorporating magnetization [56], longitudinal expansion [59, 60], and rotating solutions [61]. Concurrently, efforts to address causality and stability in relativistic dissipative MHD through the Israel-Stewart formalism have help gain advanced understanding of non-resistive magnetohydrodynamic behaviors [62−66].

Thermal photons (and dileptons) serve as one of the cleanest probes of QGP properties [67−75]. They are emitted throughout all stages of heavy-ion collisions and escape the medium without significant reabsorption. Originating from initial hard scatterings, medium-induced thermal radiation, and late-stage hadronic decays, they carry useful information about the thermodynamic and dynamical history of the QGP [73, 76−80]. Recent studies highlight their utility in probing the initial states of the fireball [81], measuring transport coefficients such as shear/bulk viscosity, and extending the knowledge of the differential emission rates from a strongly magnetized plasma [75]. Thermal photon spectra depend on QGP temperature evolution, which is governed by relativistic hydrodynamics with appropriate initial conditions. Key production mechanisms include quark-antiquark annihilation ($q\bar{q} \to g\gamma$), Compton scattering ($q(\bar{q})g \to q(\bar{q})\gamma$), bremsstrahlung processes, and soft processes calculated within hard thermal loop perturbation theory [67, 73, 77, 78, 82, 83]. Their contributions vary across momentum ranges, and they encode the details of the electromagnetic response of the medium.

Against this backdrop, this study investigates thermal photon production in the QGP stage under external magnetic fields within an ideal magnetohydrodynamic framework. Building on the Victor-Bjorken flow assumptions [55, 56, 84], we analyze how magnetic field dynamics characterized by a power-law decay $\vec{B}(\tau) = \vec{B}_0(\tau_0/\tau)^a$ with decay parameter a and initial strength parameter σ modulate the QGP temperature evolution and subsequent photon emission. We calculate photon production rates for three dominant processes: Compton scattering with $q\bar{q}$ annihilation (C+A), bremsstrahlung (Bre), and $q\bar{q}$ annihilation with additional scattering (A+S), integrating these rates over the spacetime history of the QGP to obtain observable spectra. We systematically vary a and σ and quantify how magnetic field decay kinetics and initial strength influence photon yields across transverse momentum ranges, rapidity intervals, and temporal stages of QGP evolution. This study not only extends previous analyses of photon production in viscous and accelerated fluids to the magnetohydrodynamic [85] regime but also establishes a foundational framework for future investigations into magnetization, dissipative effects [67] and spin-dependent phenomena [79, 86] in relativistic heavy-ion collisions.

The remainder of this paper is organized as follows: In Sec. II, we introduce the MHD framework and photon rate formalisms. In Sec. III, we present the results for photon production. Finally, we provide a summary in Sec. IV. Throughout this work, $u^\mu = \gamma\left(1, \vec{v}\right)$ is the four-velocity field that satisfies $u^\mu u_\mu = 1$, and the spatial projection operator $\Delta^{\mu\nu} = g^{\mu\nu} - u^\mu u^\nu$ is defined with the Minkowski metric $g^{\mu\nu} = \mathrm{diag}(1,-1,-1,-1)$. It is worth noting that the orthogonality relationship $\Delta^{\mu\nu}u_\nu = 0$ is satisfied.

II. FORMALISM

A. Magnetohydrodynamic framework

The total energy-momentum tensor of relativistic fluids in the presence of magnetic fields is described by the causal second-order Israel-Stewart (IS) theory. This theory is a key framework for capturing dissipative effects in relativistic systems while ensuring causality and stability [62, 87].

$$T^{\mu\nu} = (\varepsilon + p + \Pi + E^2 + B^2)u^\mu u^\nu - \left(p + \Pi + \frac{1}{2}E^2 + \frac{1}{2}B^2\right)g^{\mu\nu} - E^\mu E^\nu - B^\mu B^\nu - u^\mu \epsilon^{\nu\lambda\alpha\beta}E_\lambda B_\alpha u_\beta - u^\nu \epsilon^{\mu\lambda\alpha\beta}E_\lambda B_\alpha u_\beta + \pi^{\mu\nu}, \tag{1}$$

where ε and p represent the energy density and pressure, u^μ is the fluid four-velocity, $\pi^{\mu\nu}$ represents the shear viscous tensor, and Π is the bulk viscous pressure. The magnetic (B^μ) and electric (E^μ) field four-vectors are defined as

$$B^\mu = \frac{1}{2}\epsilon^{\mu\nu\alpha\beta}u_\nu F_{\alpha\beta}, \quad E^\mu = F^{\mu\nu}u_\nu, \tag{2}$$

with $F^{\mu\nu} = \partial^\mu A^\nu - \partial^\nu A^\mu$ (Faraday tensor, encoding electromagnetic field dynamics) and $\epsilon^{\mu\nu\alpha\beta}$ (Levi-Civita tensor, with $\epsilon^{0123} = +1$ for orientation). These fields satisfy $u^\mu E_\mu = u^\mu B_\mu = 0$, confirming their spacelike nature, and $B^\mu B_\mu = -B^2$, $E^\mu E_\mu = -E^2$, span> B and E are field magnitudes.

In the non-resistive limit (infinite electrical conductivity σ_{el}), the electric field $E^\mu \to 0$ to ensure finite charge current $j^\mu = \sigma_{el}E^\mu$, which is a key constraint for ideal MHD [55]. Here, magnetic field evolution is governed by $\partial_\nu(B^\mu u^\nu - B^\nu u^\mu) = 0$, reflecting the "frozen-flux theorem" where field lines are advected with the fluid. For ideal fluids (neglecting viscosity, $\Pi = \pi^{\mu\nu} = 0$), the energy-momentum tensor simplifies to [55, 62]

$$T^{\mu\nu} = (\varepsilon + p + B^2)u^\mu u^\nu - \left(p + \frac{1}{2}B^2\right)g^{\mu\nu} - B^\mu B^\nu. \quad (3)$$

The system evolves via energy-momentum conservation to

$$\partial_\mu T^{\mu\nu} = 0. \quad (4)$$

To close the equations, we adopt a conformal equation of state (EoS) for high-temperature QGP: $\varepsilon = 3p$ (implying sound speed $c_s^2 = 1/3$). This approximation is valid for the deconfined phase where quark-gluon degrees of freedom dominate. However, we note that lattice QCD calculations predict a temperature-dependent $c_s(T)$ for a more realistic description. In addition, we neglect QGP magnetization [56], assuming isotropic pressure and no magnetic-field-induced modifications to the EoS.

Under longitudinal boost invariance-appropriate for high-energy heavy-ion collisions where the fireball expands along the beam axis, we use Milne coordinates $t = \tau\cosh\eta_s$ and $z = \tau\sinh\eta_s$. Here, $\tau = \sqrt{t^2 - z^2}$ represents the proper time (invariant under longitudinal boosts) and $\eta_s = 0.5\ln[(t+z)/(t-z)]$ is the space-time rapidity. The fluid four-velocity takes the form

$$u^\mu = (\cosh\eta_s, 0, 0, \sinh\eta_s) = \gamma(1, 0, 0, z/t), \quad (5)$$

with $\gamma = \cosh\eta_s$ as the Lorentz factor, capturing relativistic effects in the longitudinal direction.

Following Refs. [55, 56, 59, 62], the magnetic field is assumed to decay via a power law in proper time as

$$\overrightarrow{B}(\tau) = \overrightarrow{B}_0\left(\frac{\tau_0}{\tau}\right)^a, \quad (6)$$

where $a > 0$ is the decay constant (controlling decay rate), τ_0 represents the initial proper time, and $B_0 \equiv B(\tau_0)$ is the initial field strength.

Projecting $\partial_\mu T^{\mu\nu} = 0$ onto the fluid four-velocity u_μ (Landau-Lifshitz frame, where energy flow is measured in the fluid rest frame) gives the energy conservation equation

$$\frac{\partial\left(\varepsilon + \frac{1}{2}B^2\right)}{\partial\tau} + \frac{\varepsilon + p + B^2}{\tau} = 0, \quad (7)$$

with $u\cdot\partial = \partial/\partial\tau$ (time derivative in the fluid frame), $\partial_\mu u^\mu = 1/\tau$ (expansion factor, reflecting longitudinal dilution), and $\nabla^\mu = \Delta^{\mu\nu}\partial_\nu$ (spatial gradient operator) [88, 89].

Projecting orthogonally to u^μ via

$$\Delta_{\mu\nu}\partial_\alpha T^{\alpha\nu} = 0, \quad (8)$$

yields the momentum conservation equation

$$\nabla^\mu\left(p + \frac{B^2}{2}\right) - (\varepsilon + p + B^2)\frac{\partial u^\mu}{\partial\tau} = 0. \quad (9)$$

For the space-time rapidity component $\mu = \eta_s$, this simplifies to

$$\frac{\partial}{\partial\eta_s}\left(p + \frac{1}{2}B^2\right) = 0, \quad (10)$$

This implies that thermodynamic variables are uniform in η_s (spatially homogeneous) and depend solely on τ [55, 89]. Transverse velocities (in x,y directions) remain zero because of initial symmetry as no net forces are generated to induce motion.

For simplicity, we use the following thermodynamic relationships [55, 56, 89].

$$p = a_1 T^4, \quad p = c_s^2\varepsilon = \varepsilon/3, \quad B_0^2 = \sigma T_0^4, \quad (11)$$

where T_0 represents the initial temperature at τ_0, and

$$a_1 = \left(16 + \frac{21}{2}N_f\right)\frac{\pi^2}{90} \quad (12)$$

is a constant determined by the number of quark flavors N_f and gluon colors. The dimensionless parameter σ characterizes initial magnetic field strength. For RHIC energies ($T_0 = 0.31$ GeV) with $B_0 \in [10^{18}, 10^{19}]$ Gauss (generated by rapid motion of charged spectator nucleons), results in σ ranges from 0.04 to 40. Notably, $B_0^2 = \sigma T_0^4$ is an effective estimation of the initial magnetic field strength based on vacuum calculations for relativistic heavy-ion collisions [55, 56] valid for central-to-moderately non-central collisions in the ideal MHD limit. This relationship fails for finite QGP conductivity, magnetized QGP, or ultra-peripheral collisions, where the initial field depends strongly on the impact parameter b and requires spatial-resolved calculations.

B. Analytical solution for the MHD flow

We begin by analyzing the 1+1 dimensional ideal MHD flow-known as the *Victor-Bjorken* flow [55]. This is a model for describing longitudinal expansion in high-energy heavy-ion collisions. This model simplifies the problem by assuming boost invariance along the beam axis, making it tractable for exploring magnetic field effects on QGP evolution. Starting from the energy conservation equation (Eq. (7)), we incorporate contributions from the external magnetic field and utilize the thermodynamic relationships from Eq. (11) (*e.g.*, $p = a_1 T^4$ and $B_0^2 = \sigma T_0^4$) to derive a temperature-dependent form of the conservation law. This reduces to

$$\frac{\partial T}{\partial \tau}+\frac{(1-a)\sigma T_0^4}{12a_1T^3}\left(\frac{\tau_0}{\tau}\right)^{2a}\frac{1}{\tau}+\frac{T}{3\tau}=0. \tag{13}$$

Here, the first, second, and third terms represent the local rate of temperature change, influence of the magnetic field (via σ and decay parameter a), and longitudinal expansion (consistent with Bjorken scaling). The analytical solution to this equation is

$$T=T_0\left(\frac{\tau_0}{\tau}\right)^{\frac{1}{3}}\left[1+\frac{\sigma(a-1)}{2a_1(3a-2)}\left(1-\left(\frac{\tau_0}{\tau}\right)^{2a-\frac{4}{3}}\right)\right]^{\frac{1}{4}}. \tag{14}$$

This solution combines two key components: the standard Bjorken-like decay $\propto(\tau_0/\tau)^{1/3}$ and a magnetic field correction term, which modifies the temperature based on σ and a.

The upper panel of Fig. 1 illustrates temperature T as a function of proper time τ for $\sigma=2$, with varying magnetic field decay parameters $a=0.5$, 1, 2, 5 (initial conditions: $\tau_0=0.5$ fm/c, $T_0=0.6$ GeV). For $a>0$, a clear trend emerges: the normalized temperature decays more slowly with increasing a . This behavior can be attributed to the faster magnetic field decay (larger a) transferring energy from the field to the QGP more efficiently, which is a process referred to as the "reheating" of the energy density [55]. For example, $a=5$ (rapid decay) retains higher temperatures than $a=0.5$ (slow decay) at late times becuase the energy of the field is deposited into the medium before being cooled by the significant expansion.

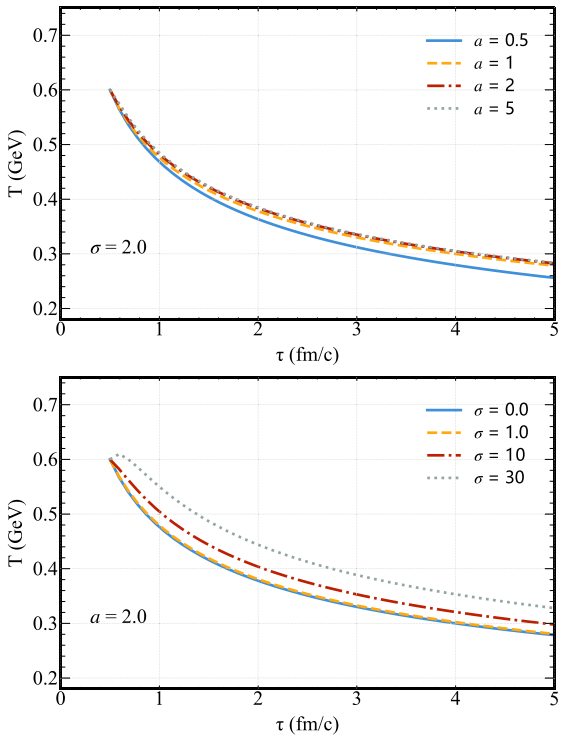

Fig. 1. (color online) Evolution of temperature T (Eq. (14)) for a magnetic field with functions of proper time τ for different initial magnetic field (upper panel) and different magnetic field decay parameter a (lower panel).

The lower panel of Fig. 1 plots $T(\tau)$ for a fixed decay parameter $a=2$ and varying initial magnetic field strengths $\sigma=0.01$, 1, 10, 30. A larger σ (stronger initial field) slows the decay of T, with the most pronounced effect for $\sigma=30$. The magnetic correction term in Eq. (14) is non-monotonic in τ, which leads to an initial "reheating" spike for sufficiently large σ (*e.g.*, $\sigma=30$). This spike occurs because the strong initial field releases energy into the QGP faster than the expansion can cool it, temporarily reversing the temperature decay.

Consistent with prior studies [55, 56, 84], we examine the divergent behavior of Eq. (14) under specific limits of a, which govern the decay rate of the magnetic field and its coupling to the QGP.

Case A For $a=1$ (ideal MHD limit with infinite conductivity, corresponding to maximal magnetic induction), the magnetic field is "frozen" into the fluid, and the correction term in Eq. (14) vanishes. This reduces the solution to the standard Victor-Bjorken flow [55].

$$T=T_0\left(\frac{\tau_0}{\tau}\right)^{\frac{1}{3}}. \tag{15}$$

Here, the magnetic field does not modify the temperature decay because energy transfer between the field and fluid is balanced by the expansion.

Case B In the limit $a\to\frac{2}{3}$, the correction term in Eq. (14) simplifies via L'Hospital's rule, yielding a logarithmic dependence

$$\lim_{a\to\frac{2}{3}}\frac{\sigma(a-1)}{2a_1(3a-2)}\left(1-\left(\frac{\tau_0}{\tau}\right)^{2a-\frac{4}{3}}\right)=\frac{\sigma}{9a_1}\ln\left(\frac{\tau_0}{\tau}\right). \tag{16}$$

Collecting the terms, the temperature evolution becomes

$$T=T_0\left(\frac{\tau_0}{\tau}\right)^{\frac{1}{3}}\left[1+\frac{\sigma}{9a_1}\ln\left(\frac{\tau_0}{\tau}\right)\right]^{\frac{1}{4}}. \tag{17}$$

For $\tau>\tau_0$, the logarithmic term is negative (since $\ln(\tau_0/\tau)<0$), reducing T and accelerating its decay. This reflects a regime where magnetic field decay drains energy from the QGP faster than only expansion, enhancing cooling.

Case C For $a\to\infty$ (super-fast magnetic field decay), the field dissipates almost instantaneously, depositing its

energy into the QGP early in the evolution. In this limit,

$$\lim_{a\to\infty}\frac{\sigma(a-1)}{2a_1(3a-2)}\left(1-\left(\frac{\tau_0}{\tau}\right)^{2a-\frac{4}{3}}\right)=\frac{\sigma}{6a_1}. \tag{18}$$

The temperature evolution simplifies to

$$T=T_0\left(\frac{\tau_0}{\tau}\right)^{\frac{1}{3}}\left(1+\frac{\sigma}{6a_1}\right)^{\frac{1}{4}}. \tag{19}$$

Here, the super-fast field decay slows temperature decay by adding a constant offset to the Bjorken term, establishing an upper bound on T for a given σ. This behavior aligns partially with current magnetic field evolution models, particularly for $a \geqslant 1$, where the field decay efficiently reheats the QGP.

In the upper panel of Fig. 2, we present temperature T as a function of proper time for the specified limit $a \to 2/3$ (Eq. (17)) with various σ = 0, 1, 10, and 20. As already analyzed in the previous section, for $\tau > \tau_0$, the log term reduces the value of T_0, leading to a faster decrease in temperature when compared with the ideal-MHD limit ($\sigma = 0.0$). This is presented with a solid-blue line. Furthermore, it is clear that larger values of σ will lead to a faster decrease in T (note that for $\sigma = 20$, $T \approx 0$ at $\tau = 3.2$ fm).

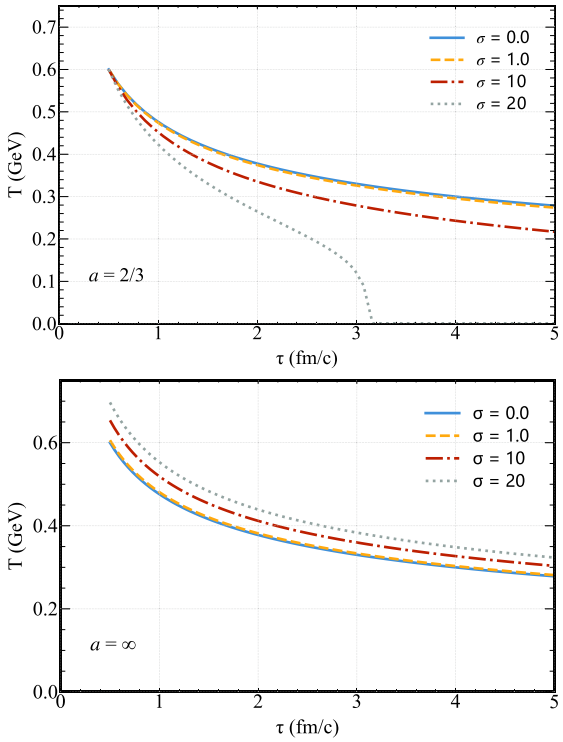

Fig. 2. (color online) Evolution of temperature T as functions of proper time τ for different values of the initial magnetic field decay parameter a and strength σ.

In the lower panel of Fig. 2, we plot the evolution of temperature T in the case $a \to \infty$ (Eq. (19)). Further, in this case, different lines refer to different levels of the initial magnetization strength σ. The second term $(1+\sigma/6a_1)$ in Eq. (19) is always positive for the positive σ; therefore, the evolution of the temperature is expected to be slower than that in the standard ideal-MHD limit.

In Fig. 3, we show the evolution of temperature T in the different limit cases (Eqs. (14), (17), and (19)); however, we fix the initial magnetization to $\sigma = 2$. We show the evolution for $a = 2/3$, $a = 1$, $a = 5$ and $a = \infty$. Clearly, T decreases more rapidly for $a = 2/3$ when compared to that for case $a = 1$, whereas for $a = 5$ it decreases more slowly and almost decays asymptotically at the same rate as that for the $a = \infty$ case.

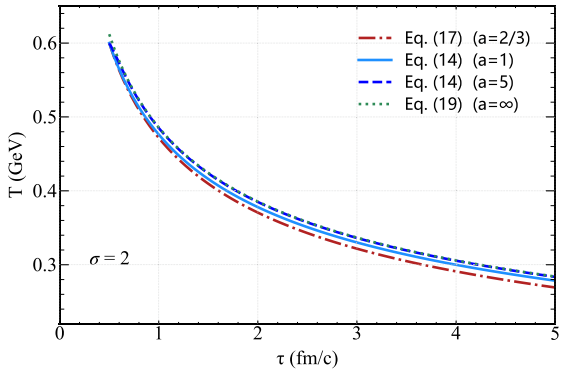

Fig. 3. (color online) Evolution of temperature T as a function of proper time τ for different limits of magnetic field decay parameter a with $\sigma = 2$.

C. Thermal photons

Thermal photons emitted during the QGP phase serve as critical probes of the thermodynamic and dynamical properties of the medium because they escape the QGP without significant reabsorption, carrying unaltered information about their production environment. These photons originate from several key QCD processes. The primary mechanisms include Compton scattering ($q(\bar{q})g \to q(\bar{q})\gamma$), where a quark (or antiquark) scatters off a gluon and emits a photon, and quark-antiquark annihilation ($q\bar{q} \to g\gamma$), where a quark-antiquark pair annihilates into a gluon and a photon [73, 82].

Higher-order processes play a non-negligible role: Aurenche *et al.* demonstrated that two-loop bremsstrahlung (radiation from charged particles accelerating in strong fields) contributes to photon production at a magnitude comparable to that of one-loop Compton scattering or annihilation [67, 73]: one channel for hard photon emission involving the annihilation of off-shell quarks and antiquarks, accompanied by interactions with

additional quarks or gluons-processes that become significant in the dense, high-temperature QGP environment. Although early studies of photon production in heavy-ion collisions focused predominantly on Compton scattering and $q\bar{q}$ annihilation, many studies emphasized the need to incorporate these higher-order contributions to accurately describe experimental observations [67, 73, 82].

We adopt one-loop perturbative QCD calculations supplemented with a hard thermal loop (HTL) resummation to quantify thermal photon production. This technique accounts for medium effects (*e.g.*, screening of color charges) in the QGP [82]. This framework yields the following production rates for the dominant processes.

Compton scattering + $q\bar{q}$ *annihilation* (C+A): This channel combines contributions from quark-gluon Compton scattering and quark-antiquark annihilation described by

$$E\frac{\mathrm{d}N_{\mathrm{C+A}}}{\mathrm{d}^3p\mathrm{d}^4x}=\frac{1}{2\pi^2}\alpha\alpha_s\left(\sum_f e_f^2\right)T^2\mathrm{e}^{-E/T}\ln\left(\frac{cE}{\alpha_s T}\right), \quad (20)$$

where $\alpha=1/137$ is the electromagnetic fine-structure constant, α_s represents the strong coupling constant, and e_f denotes the electric charge of quark flavor f (in units of the electron charge e). For this study, we consider light quarks (u and d) with $e_u=2/3$ and $e_d=-1/3$. The constant $c\approx 0.23$ arises from HTL resummation, and the exponential factor $\mathrm{e}^{-E/T}$ reflects the Boltzmann distribution of thermal particles in the QGP. The strong coupling is parametrized as a function of temperature [90].

$$\alpha_s(T)=\frac{6\pi}{(33-2N_f)\ln(8T/T_c)}, \quad (21)$$

where $N_f=2$ (number of active quark flavors), $T_c=0.14$ GeV (QGP-hadron phase transition temperature), and the logarithmic dependence captures the running of α_s with the energy scale.

Bremsstrahlung (Bre) processes: Bremsstrahlung describes photon emission from quarks accelerated by interactions with other partons (quarks or gluons) in the QGP. Its rate is given by

$$E\frac{\mathrm{d}N_{\mathrm{Bre}}}{\mathrm{d}^3p\mathrm{d}^4x}=\frac{1}{8\pi^5}\alpha\alpha_s\left(\sum_f e_f^2\right)\frac{T^4}{E^2}\mathrm{e}^{-E/T}(J_T-J_L)I(E,T), \quad (22)$$

where $J_T\approx 1.11$ and $J_L\approx -1.06$ are transverse and longitudinal flow parameters, respectively, determined from two loop calculations for two quark flavors and three gluon colors [73, 91]. The function $I(E,T)$ encapsulates kinematic effects via polylogarithmic terms

$$I(E,T)=3\zeta(3)+\frac{\pi^2}{6}\frac{E}{T}+\frac{E^2}{T^2}\ln 2+4\mathrm{Li}_3(-\mathrm{e}^{-|E|/T})+\frac{2E}{T}\mathrm{Li}_2(-\mathrm{e}^{-|E|/T})-\left(\frac{E}{T}\right)^2\ln\left(1+\mathrm{e}^{-|E|/T}\right), \quad (23)$$

with $\zeta(3)\approx 1.202$ (Riemann zeta function) and $\mathrm{Li}_a(z)=\sum_{n=1}^{\infty}z^n/n^a$ (polylogarithm), which describe the phase space integrals of thermal partons. The $1/E^2$ dependence reflects the soft nature of bremsstrahlung, making it dominant at low photon energies.

$q\bar{q}$-annihilation with additional scattering (A+S): This process involves quark-antiquark annihilation accompanied by a secondary scattering event in the medium, enhancing photon production at intermediate energies. Its rate is given by

$$E\frac{\mathrm{d}N_{\mathrm{A+S}}}{\mathrm{d}^3p\mathrm{d}^4x}=\frac{8}{3\pi^5}\alpha\alpha_s\left(\sum_f e_f^2\right)ET\mathrm{e}^{-E/T}(J_T-J_L). \quad (24)$$

Unlike bremsstrahlung, this channel scales linearly with photon energy E, making it more significant at a higher E than that at the Bremsstrahlung process.

In Fig. 4, we illustrate these three contributions at fixed temperatures $T=0.25$ GeV and $T=0.45$ GeV. We find that Bremsstrahlung dominates the low-energy regime, contributing up to $E\sim 1$ GeV for $T=0.25$ GeV and $E\sim 1.8$ GeV for $T=0.45$ GeV. Beyond these energies, the C+A and A+S processes become dominant because Bremsstrahlung is suppressed at the high E by the $1/E^2$ factor, while C+A and A+S processes gain strength from their logarithmic or linear dependence on E. In addition, all three rates increase with temperature, a consequence of the higher thermal occupation numbers and more frequent parton interactions in hotter QGP. This trend is consistent with previous theoretical studies [67, 73].

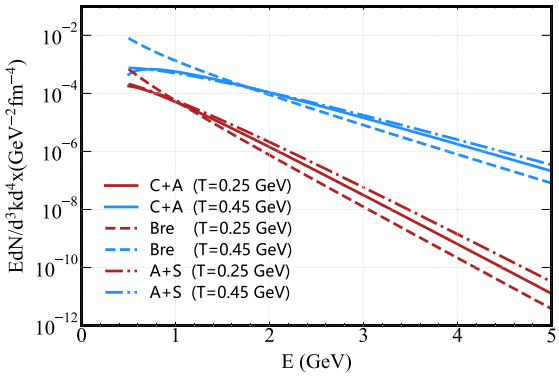

Fig. 4. (color online) Hard thermal photon rates as a function of energy E for fixed temperatures $T=0.25$ GeV and $T=0.45$ GeV, showing contributions from Compton scattering + $q\bar{q}$ annihilation (C+A), bremsstrahlung (Bre), and annihilation with scattering (A+S).

The total thermal photon rate is the sum of these individual contributions.

$$E\frac{\mathrm{d}N_{\rm total}}{\mathrm{d}^3p\mathrm{d}^4x}=E\frac{\mathrm{d}N_{\rm C+A}}{\mathrm{d}^3p\mathrm{d}^4x}+E\frac{\mathrm{d}N_{\rm Bre}}{\mathrm{d}^3p\mathrm{d}^4x}+E\frac{\mathrm{d}N_{\rm A+S}}{\mathrm{d}^3p\mathrm{d}^4x}. \tag{25}$$

In Fig. 5, we plot this total rate for $T=0.25$ GeV, $T=0.45$ GeV, and $T=0.65$ GeV, emphasizing the strong temperature dependence of photon production: at $E\sim 3$ GeV, the rate for $T=0.65$ GeV is approximately 10^4 times larger than that for $T=0.25$ GeV. This enhancement underscores the sensitivity of thermal photon spectra to the temperature evolution of the QGP as a key motivation for using photons to probe the thermal history of the medium.

To connect these differential rates to observable spectra, we integrate the total rate over the QGP's spacetime evolution, following the approach in Refs. [67, 73, 82].

$$\left(\frac{\mathrm{d}}{\mathrm{d}^2p_{\rm T}\mathrm{d}y}\right)_{y,\,p_{\rm T}}=Q_c\int_{\tau_0}^{\tau_f}\mathrm{d}\tau\,\tau\int_{-y_{\rm nuc}}^{y_{\rm nuc}}\mathrm{d}\eta_s\left(E\frac{\mathrm{d}N_{\rm total}}{\mathrm{d}^3p\mathrm{d}^4x}\right), \tag{26}$$

where $\tau_0=0.5$ fm/c (initial proper time) and τ_f is freeze-out proper time, when the QGP cools to $T_c=140$ MeV. The integral over τ accounts for photon production throughout the lifetime of the QGP, and it is weighted by the expansion factor τ (a consequence of longitudinal boost invariance) while the integral over η_s (space-time rapidity) spans the nuclear rapidity range $y_{\rm nuc}$. The factor $Q_c\sim 180$ fm^2 is the nuclear cross-section for Au+Au collisions [67, 73, 82, 91].

Within the Victor-Bjorken flow framework (neglecting transverse expansion), the fluid four-velocity is $u^\mu=(\cosh\eta_s,0,0,\sinh\eta_s)$, and the photon energy in the QGP rest frame is $E=p_T\cosh(y-\eta_s)$, where p_T and y represent the transverse momentum and photon rapidity, respectively. This relationship links the observed momentum of the photon to its energy in the medium, enabling the transformation from theoretical rates to experimental observables.

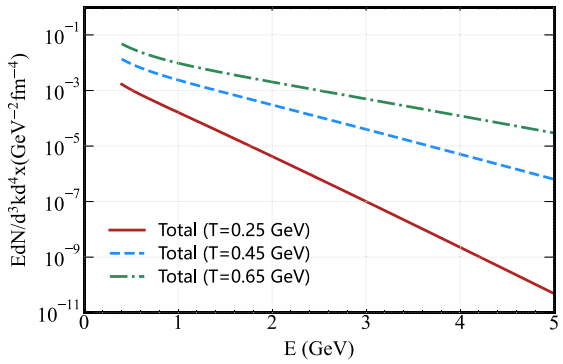

Fig. 5. (color online) Total hard thermal photon rates (Eq. (25)) as a function of energy E for $T=0.25$ GeV, $T=0.45$ GeV, and $T=0.65$ GeV, where "Total=(C+A)+Bre+(A+S)".

It is important to note the limitations of the current framework: (1) We focus on ideal MHD evolution and neglect dissipative corrections to the distribution function from viscosity or electromagnetic fields [67, 92], which could modify photon rates at late times. (2) The thermal photon production in the hot hadron gas phase, which contributes to low-p_T spectra after QGP freeze-out [73, 76, 80]. This approach focuses on the macroscopic thermodynamic modulation of the QGP by magnetic fields, which is complementary to quantum field theory based treatments that capture microscopic quantum corrections (*e.g.*, vertex/propagator modifications) to emission rates [86, 92, 93]. The magnetic field-induced modifications to parton interactions along with these complementary effects will be explored in future work to provide a more comprehensive description of thermal photon production in heavy-ion collisions.

III. RESULTS AND DISCUSSION

In this section, we investigate the effect of the external magnetic field on MHD evolution and subsequent thermal photon rate spectra. We can calculate the photon production rates after we generate the temperature profile from the MHD. The total thermal photon spectrum is obtained by adding different rates using Eqs. (20), (22), and (24) and convoluting with the space time evolution of the heavy-ion collision with Eq. (26). The final proper time τ_f is the time where the QGP temperature evolves to the freeze-out temperature T_f. For simplicity, we follow the Refs. [67, 73, 82] and consider photon production in the mid-rapidity region ($y=0$) in all calculations. In the following calculation, we use the values for the RHIC experiment given as $T_0=0.31$ GeV (initial temperature), $T_f=0.14$ GeV, $\tau_0=0.5$ fm, and $y_{\rm nuc}=5.3$, which can be obtained from Refs. [67, 73].

In Fig. 6, we present the photon rate calculated from a different source. The temperature profiles are obtained from the MHD solution given by Eq. (14) using the external magnetic field decay parameter $a=2$ and strength parameter $\sigma=2$. We find that Bremsstrahlung (Bre) contributes to the photon rate up to $p_T\sim 0.6$ GeV, and the Compton scattering with $q\bar{q}-$annihilation (C+A) and annihilation with scattering processes (A+S) play the dominant role. Further, we plot the total photon production rate and find the rate close to the A+S distribution in the high p_T region.

In Fig. 7, we plot the photon rate for initial magnetic field strengths $\sigma=0,1,10,30$ with the magnetic field decay parameter $a=2$, where the temperature profiles are obtained from the MHD solution given by Eq. (14). A strong initial magnetic field ($\sigma=30$) leads to a noticeable enhancement in the photon rate across the entire p_T

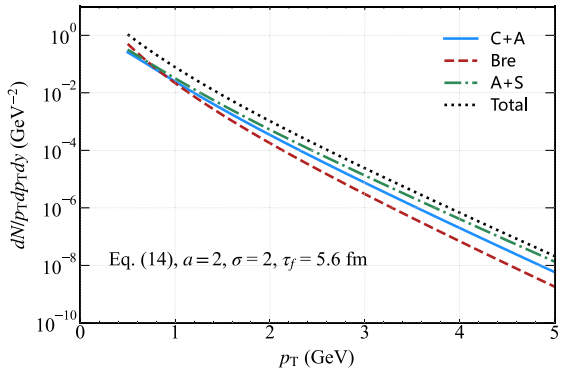

Fig. 6. (color online) Hard thermal photon spectrum from the QGP in the presence of an external magnetic field (with decay parameter $a=2$ and initial strength parameter $\sigma=2$). This shows contributions from Compton scattering + $q\bar{q}$ annihilation (C+A), bremsstrahlung (Bre), annihilation with scattering (A+S), and the total yield.

range. This behavior can be attributed to the external magnetic field exerting a slowing effect on the temperature evolution of the QGP, as clearly shown in Fig. 1. This prolongs the effective time window for thermal photon emission. In contrast, for weak magnetic fields (*e.g.*, $\sigma=1$), the effect on the photon rate is negligible. The resulting spectrum is nearly identical to that of the field-free case ($\sigma=0$) because the magnetic forces are too weak to significantly perturb the thermal dynamics of the QGP. This observation underscores that the strength of the initial magnetic field plays an important role in shaping the electromagnetic signatures of the QGP.

In Fig. 8, we present the photon spectrum with the magnetic field strength parameter $\sigma=10$ and varying decay parameters $a=0.5$, 1, 2, 5. The more pronounced splitting in the large p_T region for $a=1$, 2, 5 can be attributed to the distinct temporal evolution of the magnetic field. Larger decay parameters (*e.g.*, $a=5$) correspond to faster magnetic field decay, which indicates that the magnetic field exerts a more intense influence in the early stages of QGP evolution, when temperatures are higher and hard scattering processes (responsible for large p_T photons) are more active. In contrast, a smaller a (slower decay) leads to a more prolonged but weaker magnetic effect. For large p_T photons predominantly produced via high-momentum transfer processes sensitive to the early, high-temperature phase of QGP, the differing timing and intensity of magnetic field effects caused by varying a values result in more significant discrepancies in their production rates. This amplifies the splitting observed in the large p_T region for $a=1$, 2, 5.

In the upper panel of Fig. 9, we present the photon spectrum for varying initial magnetic field strength parameters $\sigma=0.0$, 1.0, 10, 20 with the magnetic field decay parameter fixed at $a=2/3$. The temperature profiles are derived from the corresponding MHD solutions (*e.g.*, Eq. (17) as applicable). A clear trend emerges: as σ increases, the photon yield across the p_T spectrum decreases. For the magnetic field decay parameter $a=2/3$, the thermal-photon spectrum variations are governed by initial magnetic field strength σ. Physically, $a=2/3$ lies within $0<a\leqslant\dfrac{1+c_s^2}{2}$ (where c_s^2 represents the speed of sound), wherein the fluid expends additional energy density to expel the magnetic field [55, 56]. A larger σ requires more energy compensation, accelerating the drop in temperature. Thus, the photon yield for $a=2/3$ decreases with increasing σ, contrasting with the previous $a\neq 2/3$. This temperature-driven spectrum modulation is a universal feature in Victor-Bjorken-type ideal fluids [55, 56], accelerated MHD [59], and viscous MHD systems [84]. This feature confirms the robustness of the physical mechanism.

In the lower panel of Fig. 9, we show the photon spectrum under the same set of initial magnetic field

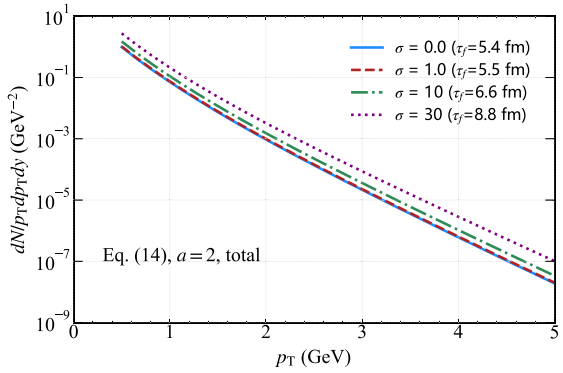

Fig. 7. (color online) Hard thermal photon spectrum from the QGP in the presence of an external magnetic field. This spectrum shows the total yield for different initial magnetic field strength parameters $\sigma=0.0$, 1.0, 10, 30 with a fixed decay parameter $a=2$ as a function of transverse momentum p_T.

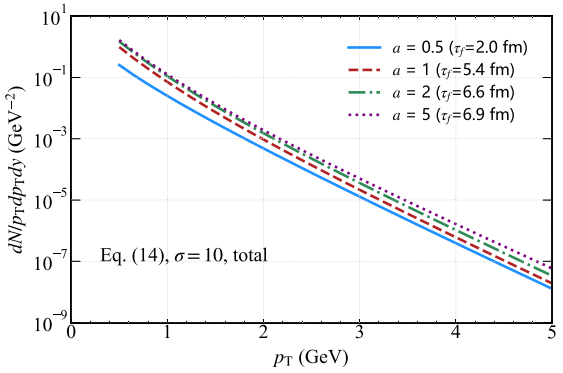

Fig. 8. (color online) Hard thermal photon spectrum from the QGP in the presence of an external magnetic field. This shows the total yield for different initial magnetic field decay parameter $a=0.5$, 1, 2, 5 with a fixed strength parameter $\sigma=10$ as a function of transverse momentum p_T.

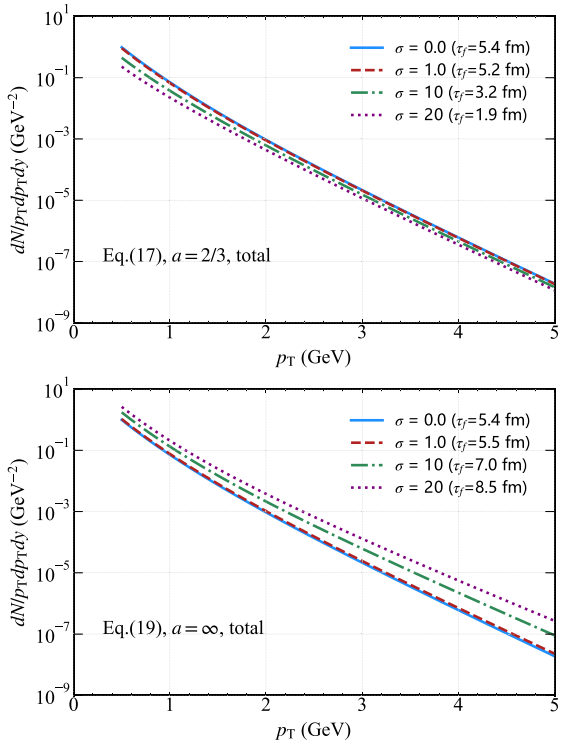

Fig. 9. (color online) Hard thermal photon spectra from the QGP in the presence of an external magnetic field. Upper panel: Total yield for different initial magnetic field strength parameters $\sigma = 0.0, 1.0, 10, 20$ with magnetic field decay parameter $a = 2/3$ (Eq. (17)). Lower panel: Total yield for the same σ values with magnetic field decay parameter $a = \infty$ (Eq. (19)).

strength parameters $\sigma = 0.0, 1.0, 10, 20$ but with the magnetic field decay parameter $a = \infty$ (Eq. (19)). In contrast to the $a = 2/3$ case, a reverse trend is observed: larger σ values lead to higher photon yields across the p_T spectrum. This can be attributed to the decay nature of the magnetic field (as $a = \infty$ implies super fast decay) exerting an enhancing effect on the thermal and dynamical processes of the QGP, promoting photon production. The contrasting dependencies of the photon yield on σ between the two figures highlight the critical role of the magnetic field decay parameter a in mediating the influence of the initial magnetic field strength on the QGP photon emission.

In Fig. 10, we present the thermal photon spectra for varying magnetic field decay parameters $a = 2/3, 2, \infty$ with fixed initial magnetic field strength parameter $\sigma = 10$, alongside the spectrum for $a = 2$ and $\sigma = 0$ (ideal MHD case). The temperature profiles are derived from the corresponding MHD solutions (Eqs. (14), (17), and (19), as applicable). A clear trend is observed: as the magnetic field decay parameter a increases, the photon yield across the p_T spectrum rises. This behavior is attributed to the larger a corresponding to the faster magnetic field decay, which intensifies the influence of the field in the early, high-temperature phase of QGP evolution when hard scattering processes (critical for photon production) are the most active. For $a = \infty$ with $\sigma = 10$, the photon yield is enhanced compared to that for the ideal MHD case ($a = 2$, $\sigma = 0$). This serves as an upper bound for photon production under magnetic field decay effects. In contrast, for $a = 2/3$ with $\sigma = 10$, the decay behavior of the magnetic field suppresses the photon yield relative to the $\sigma = 0$ case. This suppression stems from the slower decay rate of $a = 2/3$ perturbing the thermal dynamics of the QGP and diminishes emission processes.

In Fig. 11, we present the thermal photon spectra for different proper time intervals [(0.5, 1.5) fm/c, (1.5, 2.5) fm/c, (2.5, 3.5) fm/c, (3.5, 5.5) fm/c] under the condition of magnetic field decay parameter $a = 2$ and initial strength parameter $\sigma = 10$. The temperature profiles are derived from the corresponding MHD solution (Eqs. (14)). A key observation is that low p_T photons receive contributions from all stages of QGP evolution. This is because low-momentum photons are predominantly produced via relatively low-energy scattering processes,

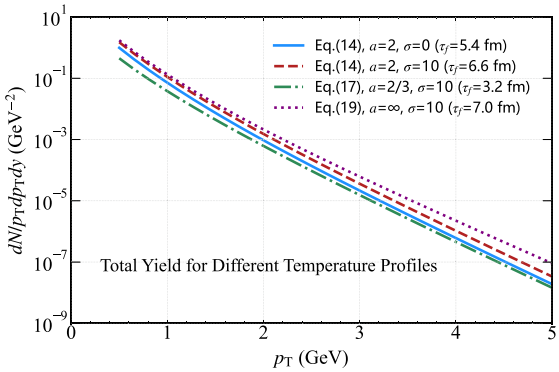

Fig. 10. (color online) Hard thermal photon spectrum from the QGP in the presence of an external magnetic field. This shows the total yield for different magnetic field decay parameters: $a = 2/3$ (Eq. (17), $\sigma = 10$), $a = 2$ (Eq. (14), $\sigma = 10$ and $\sigma = 0$), and $a = \infty$ (Eq. (19), $\sigma = 10$).

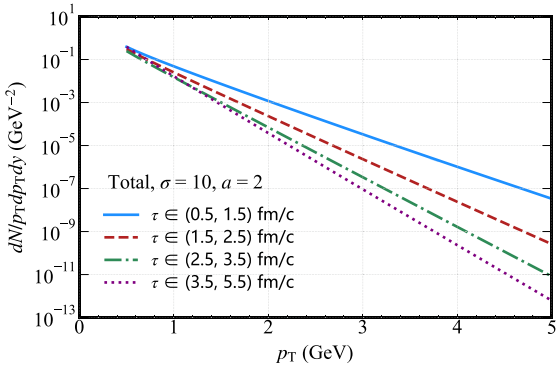

Fig. 11. (color online) Hard thermal photon spectrum from the QGP in the presence of an external magnetic field. This shows the total yield and contributions from different proper time (τ) intervals.

which remain active across the entire lifetime of the QGP as long as the system maintains sufficient temperature. In contrast, high p_T photons are primarily generated in the early stages of QGP evolution (specifically the (0.5, 1.5) fm/c interval). This behavior is cuased by high p_T photons requiring high-momentum transfer processes, which are the most efficient during the early, high-temperature phase of the QGP where the collision rate and thermal energy are the highest.

Finally, in Fig. 12, we plot the thermal photon spectra for different rapidity intervals [$\eta_s \in$(0.0, 1.0), $\eta_s \in$ (1.0, 2.0), $\eta_s \in$ (2.0, 3.0)] under the conditions of magnetic field decay parameter $a = 2$ and initial strength parameter $\sigma = 10$. A distinct feature is observed for the photons at $y = 0$: the yield is predominantly contributed by the central rapidity interval $\eta_s \in$(0.0, 1.0). This can be attributed to particle production in heavy-ion collisions being typically most intense around mid-rapidity, where the density of interacting particles and the corresponding thermal emission processes are the most active. Furthermore, a clear decreasing trend is evident with increasing rapidity: the contribution to the photon yield diminishes as the rapidity interval moves away from the center (*e.g.*, from (0.0, 1.0) to (2.0, 3.0)). This behavior aligns with the expected momentum distribution of particles in the QGP, where the number of particles with large rapidities is smallerbecuase of the kinematic constraints of the collision system. These results highlight the sensitivity of thermal photon production to the rapidity distribution, with central rapidity regions playing a dominant role in shaping the overall yield at $y = 0$.

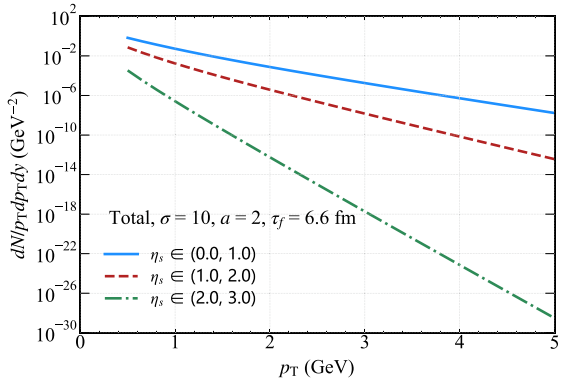

Fig. 12. (color online) Hard thermal photon spectrum from the QGP in the presence of an external magnetic field. This shows the total yield and contributions from different space-time rapidity (η_s) intervals.

IV. CONCLUSIONS

In this work, we investigated the effect of external magnetic fields on thermal photon production in the QGP within an MHD framework. We adopted the relativistic fluid theory to describe the energy-momentum tensor of the QGP in the presence of magnetic fields, simplifying it to the ideal fluid limit under the non-resistance approximation (Victor-Bjorken type). The magnetic field is assumed to decay via a power-law in proper time, $\vec{B}(\tau) = \vec{B}_0(\tau_0/\tau)^a$, where a represents the decay parameter and σ characterizes the initial field strength. Using the Victor-Bjorken flow assumption [55, 56, 84], we revisit the analytical solutions for the QGP temperature evolution (Eq. (14)). These solutions show distinct behaviors depending on a and σ. For example, a larger a or σ slows temperature decay, while $a = 2/3$ accelerates it for increasing σ [55].

Thermal photon production rates are calculated by considering three dominant processes [67, 73, 82]: Compton scattering with $q\bar{q}$ annihilation (C+A), bremsstrahlung (Bre), and $q\bar{q}$ annihilation with additional scattering (A+S). The total photon spectrum is obtained by integrating these rates over the spacetime evolution of the QGP (Eq. (26)), accounting for the temperature profiles from MHD simulations. This approach captures the contributions of different processes across momentum ranges, with Bremsstrahlung dominating low p_T and C+A/A+S dominating high p_T.

Our results reveal that the external magnetic field affects the photon spectrum: (i) Increasing the decay parameter a enhances the photon yield across all p_T, with $a = \infty$ (super-fast decay) providing an upper bound because of the intensified early-stage QGP heating. (ii) For $a = 2/3$, a larger σ suppresses yields by accelerating temperature decay, while for $a = \infty$, a larger σ enhances yields via prolonged thermal emission. (iii) Low p_T photons receive contributions from all QGP stages, whereas high p_T photons are dominated by early-time production. (iv) Central rapidity intervals (0.0, 1.0) dominate the yield at $y = 0$, with contributions diminishing for larger rapidities. These findings highlight the critical role of magnetic field dynamics in QGP electromagnetic signatures, offering insights for heavy-ion collision experiments.

This study is simple and easily reproducible and extends the studies of photon yields from viscous fluids [67, 73], Gubser flow [74], and longitudinally accelerated fluids [85] to the MHD regime. It holds many theoretical potential for further exploration, including photon yields in MHD with magnetic susceptibility [56], viscous MHD [84], longitudinally accelerated MHD [59], spin-hydrodynamics [94], and non-extensive MHD [95]. Such investigations are expected to help deepen our understanding of how strong magnetic fields and spin effects influence photon (or dilepton) yields in a relativistic hydrodynamic framework while providing a testbed for thermal photons (or dilepton [79, 96]) from numerical MHD simulations.

References

[1] J. Adams and others (STAR Collaboration), Nucl. Phys. A **757**, 102 (2005)
[2] K. Aamodt *et al*. (ALICE Collaboration), JINST **3**, S08002 (2008)
[3] W. T. Deng and X. G. Huang, Phys. Rev. C **85**, 044907 (2012)
[4] H. Li, X. L. Sheng, and Q. Wang, Phys. Rev. C **94**(4), 044903 (2016)
[5] U. Gursoy, D. E. Kharzeev, and K. Rajagopal, Phys. Rev. C **89**(5), 054905 (2014)
[6] Santosh K. Das, S. Plumari, S. Chatterjee *et al*., Phys. Lett. B **768**, 260 (2017)
[7] U. Gürsoy, D. E. Kharzeev, E. Marcus *et al*., Phys. Rev. C **98**(5), 055201 (2018)
[8] S. Chatterjee and P. Bozek, Phys. Lett. B **798**, 134955 (2019)
[9] L. Oliva, S. Plumari, and V. Greco, JHEP **05**, 034 (2021)
[10] Y. Sun, S. Plumari, and V. Greco, Phys. Lett. B **816**, 136271 (2021)
[11] Z. F. Jiang, S. S. Cao, W. J. Xing *et al*., Phys. Rev. C **105**(5), 054907 (2022)
[12] A. Huang, Y. Jiang, S. Shi *et al*., Phys. Lett. B **777**, 177 (2018)
[13] D. E. Kharzeev, L. D. McLerran, and H. J. Warringa, Nucl. Phys. A **803**, 227 (2008)
[14] K. Fukushima, D. E. Kharzeev, and H. J. Warringa, Phys. Rev. D **78**, 074033 (2008)
[15] D. E. Kharzeev, J. Liao, S. A. Voloshin *et al*., Prog. Part. Nucl. Phys. **88**, 1 (2016)
[16] D. E. Kharzeev, J. Liao, and P. Tribedy, Int. J. Mod. Phys. E **33**(09), 2430007 (2024)
[17] G.-R. Liang, J. Liao, S. Lin *et al*., Chin. Phys. C **44**(9), 094103 (2020)
[18] Y. Jiang, S. Shi, Y. Yin *et al*., Chin. Phys. C **42**(1), 011001 (2018)
[19] S. Choudhury *et al*. (STAR Collaboration), Chin. Phys. C **46**(1), 014101 (2022)
[20] A. H. Tang, Chin. Phys. C **44**(5), 054101 (2020)
[21] J. H. Gao, G. L. Ma, S. Pu *et al*., Nucl. Sci. Tech. **31**(9), 90 (2020)
[22] S. Shi, Y. Jiang, E. Lilleskov *et al*., Annals Phys. **394**, 50 (2018)
[23] X. G. Huang and J. Liao, Phys. Rev. Lett. **110**(23), 232302 (2013)
[24] S. Pu, S. Y. Wu, and D. L. Yang, Phys. Rev. D **89**(8), 085024 (2014)
[25] D. E. Kharzeev and H. U. Yee, Phys. Rev. D **83**, 085007 (2011)
[26] L. Adamczyk *et al*. (STAR Collaboration), Phys. Rev. Lett. **114**(25), 252302 (2015)
[27] A. M. Sirunyan *et al*. (CMS Collaboration), Phys. Rev. C **97**(4), 044912 (2018)
[28] M. Abdallah *et al*. (STAR Collaboration), Phys. Rev. C **105**(1), 014901 (2022)
[29] M. S. Abdallah *et al*. (STAR Collaboration), Phys. Rev. Lett. **128**(9), 092301 (2022)
[30] J. Adam *et al*. (STAR Collaboration), Phys. Rev. Lett. **123**(16), 162301 (2019)
[31] S. Acharya *et al*. (ALICE Collaboration), Phys. Rev. Lett. **125**(2), 022301 (2020)
[32] M. I. Abdulhamid *et al*. (STAR Collaboration), Phys. Rev. X **14**(1), 011028 (2024)
[33] U. Heinz and R. Snellings, Ann. Rev. Nucl. Part. Sci. **63**, 123 (2013)
[34] C. Gale, S. Jeon, and B. Schenke, Int. J. Mod. Phys. A **28**, 1340011 (2013)
[35] Iu. Karpenko, P. Huovinen, and M. Bleicher, Comput. Phys. Commun. **185**, 3016 (2014)
[36] S. Jeon and U. Heinz, Int. J. Mod. Phys. E **24**(10), 1530010 (2015)
[37] F. Becattini and Iu. Karpenko, Phys. Rev. Lett. **120**(1), 012302 (2018)
[38] F. Becattini and M. A. Lisa, Ann. Rev. Nucl. Part. Sci. **70**, 395 (2020)
[39] Z. F. Jiang, C. B. Yang, M. Csanad *et al*., Phys. Rev. C **97**(6), 064906 (2018)
[40] W. Zhao, C. Shen, and B. Schenke, Phys. Rev. Lett. **129**(25), 252302 (2022)
[41] W. Zhao, C. M. Ko, Y. X. Liu *et al*., Phys. Rev. Lett. **125**(7), 072301 (2020)
[42] Z. F. Jiang, S. S. Cao, X. Y. Wu *et al*., Phys. Rev. C **105**(3), 034901 (2022)
[43] X. Y. Wu, G. Y. Qin, L. G. Pang *et al*., Phys. Rev. C **105**(3), 034909 (2022)
[44] Z. F. Jiang, S. S. Cao, and B. W. Zhang, Phys. Rev. C **111**(3), 034906 (2025)
[45] G. Inghirami, L. D. Zanna, A. Beraudo *et al*., Eur. Phys. J. C **76**(12), 659 (2016)
[46] K. Nakamura, T. Miyoshi, C. Nonaka *et al*., Phys. Rev. C **107**(1), 014901 (2023)
[47] M. Mayer, A. Dash, G. Inghirami *et al*., Phys. Rev. C **111**(4), 044908 (2025)
[48] H. T. Ding, A. Francis, O. Kaczmarek *et al*., Phys. Rev. D **83**, 034504 (2011)
[49] H.-T. Ding, O. Kaczmarek, and F. Meyer, Phys. Rev. D **94**(3), 034504 (2016)
[50] G. S. Bali, F. Bruckmann, G. Endrodi *et al*., Phys. Rev. Lett. **112**, 042301 (2014)
[51] L. G. Pang, G. Endrődi, and H. Petersen, Phys. Rev. C **93**(4), 044919 (2016)
[52] Z. F. Jiang, Z. H. Zhang, X. F. Yuan *et al*., Phys. Rev. C **110**(1), 014902 (2024)
[53] A. Huang, X. Y. Wu, and M. Huang, Phys. Rev. D **110**(9), 094032 (2024)
[54] K. Fukushima, K. Hattori, and K. Mameda, 9, (2024), arXiv: 2409.18652
[55] V. Roy, S. Pu, L. Rezzolla *et al*., Phys. Lett. B **750**, 45 (2015)
[56] S. Pu, V. Roy, L. Rezzolla *et al*., Phys. Rev. D **93**(7), 074022 (2016)
[57] I. Siddique, R. j. Wang, S. Pu *et al*., Phys. Rev. D **99**(11), 114029 (2019)
[58] H. H. Peng, S. Wu, R. j. Wang *et al*., Phys. Rev. D **107**(9), 096010 (2023)
[59] D. She, Z. F. Jiang, D. Hou *et al*., Phys. Rev. D **100**(11), 116014 (2019)
[60] M. Haddadi M., W. M. Alberico, D. She *et al*., Phys. Rev. D **102**(1), 014017 (2020)
[61] M. Shokri and N. Sadooghi, JHEP **11**, 181 (2018)
[62] R. Biswas, A. Dash, N. Haque *et al*., JHEP **10**, 171 (2020)

[63] I. Cordeiro, E. Speranza, K. Ingles *et al.*, Phys. Rev. Lett. **133**(9), 091401 (2024)
[64] Z. Fang, K. Hattori, and J. Hu, Phys. Rev. D **110**(5), 056049 (2024)
[65] G. S. Rocha, D. Wagner, G. S. Denicol *et al.*, Entropy **26**(3), 189 (2024)
[66] E. R. Most and J. Noronha, Phys. Rev. D **104**(10), 103028 (2021)
[67] J. R. Bhatt, H. Mishra, and V. Sreekanth, JHEP **11**, 106 (2010)
[68] C. Gale and Kevin L. Haglin, *Electromagnetic radiation from relativistic nuclear collisions*, pages 364–429, 6, (2003)
[69] C. Gale, *Photon Production in Hot and Dense Strongly Interacting Matter*, Landolt-Bornstein **23**, 445 (2010)
[70] D. G. d'Enterria and D. Peressounko, Eur. Phys. J. C **46**, 451 (2006)
[71] O. Linnyk, V. P. Konchakovski, W. Cassing *et al.*, Phys. Rev. C **88**, 034904 (2013)
[72] I. A. Wang, X.and Shovkovy, L. Yu *et al.*, Phys. Rev. D **102**(7), 076010 (2020)
[73] F. D. Steffen and M. H. Thoma. Phys. Lett. B, **510**, 98 (2001) [Erratum: Phys. Lett. B **660**, 604 (2008)]
[74] Lakshmi J. Naik and V. Sreekanth, Eur. Phys. J. C **85**(6), 664 (2025)
[75] X. Wang and I. Shovkovy, Eur. Phys. J. C **81**(10), 901 (2021)
[76] C. Shen, U. W. Heinz, J. F. Paquet *et al.*, Phys. Rev. C **91**(2), 024908 (2015)
[77] G. David, Rept. Prog. Phys. **83**(4), 046301 (2020)
[78] B. Schenke and M. Strickland, Phys. Rev. D **76**, 025023 (2007)
[79] X. Y. Wu, H. Gao, B. Forster *et al.*, Phys. Rev. Lett. **134**(24), 242301 (2025)
[80] R. Chatterjee, P. Dasgupta, and D. K. Srivastava, Phys. Rev. C **96**(1), 014911 (2017)
[81] V. Vovchenko, Iu. A. Karpenko, M. I. Gorenstein *et al.*, Phys. Rev. C **94**(2), 024906 (2016)
[82] C. T. Traxler and M. H. Thoma, Phys. Rev. C **53**, 1348 (1996)
[83] B. S. Kasmaei and M. Strickland, Phys. Rev. D **102**(1), 014037 (2020)
[84] Z. F. Jiang, S. Y. Liu, T. Y. Hu *et al.*, Chin. Phys. **49**(11), 114104 (2025)
[85] G. L. Kasza, *Thermal Radiation from an Analytic Hydrodynamic Model with Hadronic and QGP Sources in Heavy-Ion Collisions*, 7, (2025), arXiv: 2507.13240
[86] X. Wang and I. A. Shovkovy, Phys. Rev. D **110**(11), 116005 (2024)
[87] G. S. Denicol, X. G. Huang, E. Molnár *et al.*, Phys. Rev. D **98**(7), 076009 (2018)
[88] A. Muronga, Phys. Rev. Lett. **88**, 062302 (2002)
[89] A. Muronga, Phys. Rev. C **69**, 034903 (2004)
[90] F. Karsch, Z. Phys. C **38**, 147 (1988)
[91] D. K. Srivastava, Eur. Phys. J. C, **10**, 487 (1999) [Erratum: Eur. Phys. J. C **20**, 399 (2001)]
[92] J. A. Sun and L. Yan, Phys. Lett. B **858**, 139046 (2024)
[93] K. Hattori, H. Taya, and S. Yoshida, JHEP **01**, 093 (2021)
[94] D. L. Wang, X. Q. Xie, S. Fang *et al.*, Phys. Rev. D **105**(11), 114050 (2022)
[95] K. Shen, T. S. Biro, and E. Wang, Physica A **492**, 2353 (2018)
[96] A. Dwibedi, A. K. Panda, S. Ghosh *et al.*, *Probing Dynamical Electrical Conductivity via Dilepton Emission: A Kinetic theory approach*, 8, (2025), arXiv: 2508.16988